

Semantic segmentation for quantitative analysis and comparison of microstructures of lower bainitic and tempered martensitic steels

Xiaohan Bie^a, Manoj Arthanari^a, Evelin Barbosa de Melo^a, Baihua Ren^a, Juancheng Li^b, Stephen Yue^{a*}, Salim Brahim^{a*}, Jun Song^{a*}

^a Department of Mining and Materials Engineering, McGill University, Montréal, Québec H3A 0C5, Canada

^b Department of Mechanical Engineering, McGill University, Montréal, Québec H3A 0C5, Canada

Abstract

Lower bainite (LB) and tempered martensite (TM) are two prevailing microstructures of high-strength steels (HSS). Despite their similarity in many physical attributes, LB is reported to exhibit better performance in resisting hydrogen embrittlement (HE) than TM, a difference usually attributed to their distinction in certain microstructural features, particularly carbides. Previous studies, based on conventional methods, in comparing carbides in LB and TM are often highly localized and qualitative in nature. This study presents a convolutional neural network (CNN) based deep learning (DL) model specific for characterizing carbide precipitates in scanning electron microscopy (SEM) images of LB and TM microstructures, for quantitative and statistically robust analysis of carbides. This model is demonstrated to exhibit high accuracy and efficiency in differentiating carbides and non-carbides in SEM images. Statistical analysis based on the model reveals that carbide precipitates in LB and TM share strikingly similarities, in their volume percentages, aspect ratios, as well as sizes despite TM having more finer carbides. It was also found that carbides in both LB and TM are overall, randomly oriented, in sharp contrast to the conventional belief of carbides in LB exhibiting a single variant aligned at 60° relative to the "growth direction" of the ferrite plate. The present study highlights the effectiveness and strong capability of DL in segmenting SEM images, and as a powerful tool for microstructural characterization.

1. Introduction

High-strength steels (HSS), distinguished by their remarkable strength, e.g., often with yield strength surpassing 460 MPa [1-3], are structural materials seeing widespread usage in numerous applications such as aircraft landing gears, construction, and automotive manufacturing [4-9]. Not only are they used in critical components requiring superior strength or load-bearing capacity, but they also play a vital role in reducing the weight of components. This makes HSS of strategic importance in enhancing energy efficiency and reducing emissions and carbon footprint. Tempered Martensite (TM) and Lower Bainite (LB) [8, 10] are two microstructures commonly present in many modern high-performance steels with superior mechanical properties. Both LB and TM are produced from medium carbon alloy steels but following different heat treatment processes. TM is produced with the steel first austenitized at temperatures above 800°C, and then quenched to a temperature below the martensite start (MS) temperature, where austenite transforms into martensite, followed by tempering at elevated temperatures below the austenitizing temperature [11]. LB is a microstructure formed by austempering [8], where the steel is first austenitized above 800°C, then rapidly quenched to temperatures slightly above the MS temperature, and is held at the same temperature for a specified duration [11]. Despite the significant difference in heat treatments, LB and TM share similar physical attributes, including hardness, modulus, and yield strength [8, 12, 13]. They also exhibit great similarity in the microstructures, both encompassing laths or plates of ferrite with finely dispersed carbide precipitates [8, 14].

Despite their similarities in physical properties and microstructural characteristics, LB and TM have been found to exhibit notably different performance in certain applications. One particular case is that recent experimental works [15-19] indicated that steel with the LB microstructure shows superior performance compared to steel of similar strength but with the TM microstructure, in resistance to hydrogen embrittlement (HE), a phenomenon where a material suffers loss of ductility, toughness and premature failure when exposed to hydrogen [20, 21]. The difference in HE susceptibility between LB and TM is often attributed to their distinction in certain microstructural features, particularly carbides [17, 18]. For example, Jang et al. attributed LB's enhanced HE resistance to the presence of more finely dispersed carbides, a deduction drawn from their analysis of precipitated carbides using Electron Channeling Contrast Imaging (ECCI) images [18], stating that more finely dispersed carbides would irreversibly trap more hydrogen atoms, thereby better mitigating HE [18]. Another work by Nanninga et al. suggested that LB's better HE resistance than TM can be linked to the morphologies and distributions of carbides and ferrites [17]. These studies underscore the necessity of quantitatively analyzing carbides in LB and TM.

Conventional methods for characterizing carbides in LB and TM steels rely on techniques such as Scanning Electron Microscopy (SEM) and Transmission Electron Microscopy (TEM). Utilizing these microstructure characterization techniques, it was reported that TM displays varied orientations of carbides while carbides within LB tend to align predominantly an angle of roughly 60° relative to the "growth direction" of the

ferrite plate [22, 23]. Consequently, carbides embedded within LB are believed to exhibit greater alignment within ferrite laths than TM. This nuanced difference has been a key technique researchers employed to differentiate LB and TM in microstructure analysis [8]. However, questions remain regarding the effectiveness and reliability of such method. Previous studies [24, 25] using this method mostly relied on TEM, thus highly localized comparison of microstructural features and lacking statistic significance. Meanwhile, it was also reported that the method, being qualitative, is not always reliable [8], as the occurrence of the multiple carbide orientations is also observed in LB. These inadequacies call for a new approach able to offer quantitative and statistically robust analysis in characterizing carbides in LB and TM, for more consistent and reliable comparison of these two microstructures. In addition, the conventional methods often involve considerable manual work on the intricate images, which can be time-consuming.

In search for better solutions to address these challenges, deep learning (DL) for computer vision has emerged as a potential candidate [26]. DL has been demonstrated as a significant utility in different image processing purposes such as classifications [27, 28], and segmentations [29, 30], among others [31, 32]. It was reported that DL can surpass human experts in accuracy when classifying SEM images of different steel microstructures [33]. Equally impressive is the speed at which DL processes images, enabling the segmentation of hundreds of images within seconds [34]. Within the domain of DL for computer vision, convolutional Neural Networks (CNNs) are one prevailing category of networks [35], with many different CNNs architectures

developed for different purposes, including Le-Net, U-Net, PSPNet, among others [27-32, 36, 37]. In utilizing DL for microstructural analysis, one critical task is image segmentation [38, 39], which enables precise identification and classification of distinct phases or regions within an image, and is a fundamental process to microstructure analysis, offering detailed insights into material properties by distinguishing between key constituents such as grains, phases, and defects [38]. Particularly for the task of image segmentation, CNNs architectures such as U-Net [29] and PSPNet [30], have been developed and seen great use in image segmentation.

The present work focuses on a specific CNN architecture, namely the U-Net framework [29, 40] which has been demonstrated to exhibit great robustness and accuracy in segmenting images, particularly in delineating complex contours [35]. Based on the U-Net framework, a CNN workflow has been developed for comprehensive analysis of carbide precipitates in SEM images of LB and TM microstructures, and subsequently quantitative comparison of different attributes of carbides in these two microstructures. Besides the volumetric and geometric aspects of carbides, an alignment factor was also defined to enable quantitative characterization of carbide orientations. In the end, the results were discussed and summarized.

2. Methodology

2.1 Materials

The samples used for microstructural characterization were medium-carbon, low-alloy

steels. The relevant information and properties of the samples examined are presented in **Table 1**, while the material’s chemical composition is summarized in **Table 2**. Two sets of samples were provided with identical chemical compositions but subjected to distinct heat treatments to render the TM and LB microstructures respectively in the samples. As can be noted in **Table 1**, the tensile and yield strengths of TM samples are slightly higher than those of LB samples. Charpy impact tests were also performed, from which the impact energy which quantitatively reflects the toughness of the steel [41], was measured, with the values listed in **Table 1**. We can see that the TM samples exhibit a slighter higher impact energy level, indicative of higher toughness.

Table 1. The sample material, heat treatment, microstructures and key mechanical properties, i.e., yield strength (YS), tensile strength (TS) and Charpy impact energy at room temperature.

Material	Heat Treatment	Micro-structure	YS (MPa)	TS (MPa)	Charpy Impact Energy (J)
Medium carbon (Cr-Mo-Ni) alloy steel, with B addition	Austempered	LB	1227	1538	10.2
	Quenched & tempered	TM	1455	1553	11.2

Table 2. The chemical compositions of the steel sample. All elements are in wt%.

Element	C	Mn	P	S	Si	Al	Ni	Cr	Cu	Mo	Nb	Ti	N	B
wt%	0.44	0.94	0.005	0.005	0.17	0.025	0.16	1.48	0.04	0.19	0.05	0.01	0.005	8×10^{-4}

2.2 Sample preparation and SEM imaging

The heat-treated wire rods were sectioned to a 5 mm thick sample using a laboratory-scale precision abrasive cutter. Specimens were mounted using phenolic powder,

ground to 1200 grit emery paper by common metallography method, and then polished in 3 μm and 1 μm polishing suspension to obtain a mirror finish.

The samples were then etched in 2% Nital in a fume hood for 2–4 seconds and examined on an FEI Quanta 450 scanning electron microscope to observe the microstructures. Images were captured at multiple magnifications around the surface of the sample using the backscattered electron imaging technique [42]. A total of 37 SEM images were obtained from experiments for analyzing the steel microstructures. The microstructure revealed carbide precipitates and lath features, as shown in the sample image in **Figure 1c**. In those SEM images, the black areas are steel matrix, while the light gray areas represent carbide precipitates, predominantly identified as cementite.

2.2 Mask creation

Training the DL model starts with the creation of SEM image/mask pairs. Prior to the training process, these masks must be generated (see Step 1 shown in **Figure 1b**). Masks represent the ground truth, reflecting the manual classifications of the steel matrix and carbides in the SEM images by human experts [40]. By feeding SEM images together with their corresponding mask (i.e., SEM image/mask pairs) into the model, the DL algorithm then learns from these expert classifications, to enable the model to independently classify similar patterns in new images.

In classifying the images, an approach based on pixel intensity values was developed, where every pixel in the SEM image, ranging from 0 (black) to 255 (white) in intensity,

was analyzed. A series of benchmark intensity values were selected for the identification of carbides. The benchmark intensity is used as a threshold to classify pixels as dark (for the intensity below the threshold) and light (for the intensity above the threshold) areas, indicative of the steel matrix and carbide region background respectively (see **Figure 1c**), thus classification of a SEM image. An iterative process was carried out in collaboration with experienced metallurgists to identify the best benchmark intensity that most effectively distinguishes carbides from non-carbide regions for each SEM image, and the corresponding classification was then taken as the mask for the image. Note that in the above process, a carbide area smaller than 30 pixels was considered as background noise, and categorized as part of the steel matrix background in the mask.

2.3 CNN and U-Net architecture

The U-Net framework is the specific CNN architecture of focus in this work. Utilizing this framework, a workflow has been developed to streamline the analysis of carbide precipitates in HSS, schematically illustrated in **Figure 1b**. As seen from the workflow, after obtaining the ground-truth masks, the next step is training the DL model. As previously mentioned, only a limited number of SEM images were obtained, which is insufficient for training a machine learning model [43]. To address this limitation, data augmentation was performed to expand the data set to obtain enough images for the training and later validation tasks. It is worth noting that here the data augmentation process is possible because we have high-resolution partitionable SEM images.

The data augmentation process starts by scaling an original SEM image to 10000X magnification, followed by cropping and cutting it into images of dimensions of 480 pixels in height and 640 pixels in width (see **Figures 1c**). It is important to note that the new image acquired from cropping and cutting still contains a considerable number of carbides and steel matrix features, sufficient to ensure that the essential microstructural signature is preserved to allow later training of the model. The data were then divided into three sets, namely the training (70% of data), validation (15% of data) and testing (15% of data) sets. The image data were then input into our U-Net architecture, with the specific architecture parameters detailed in **Figure 1a**. The U-Net begins with a $96 \times 128 \times 3$ input image. The encoder progressively reduces spatial dimensions (e.g., $96 \rightarrow 48 \rightarrow 24$) while increasing feature depth (e.g., $32 \rightarrow 64 \rightarrow 128$) using 3×3 convolutions with ReLU activation and 2×2 max-pooling layers, which were utilized in the architecture to downscale the image, reducing its spatial dimensions and capturing abstract features [29]. At the bottleneck, the feature map is minimized (e.g., 6×8) with maximum depth (512 channels), bridging the encoder and decoder. The decoder reconstructs spatial dimensions via 2×2 transposed convolutions, upscaling the feature maps back to the original sizes with the spatial resolution restored [29]. The final output map, with dimensions $96 \times 128 \times 2$, classified each pixel in the original image (with a total of 96×128 pixels) as either carbides or iron-matrix. The model was trained over 120 epochs, with an epoch referring to a complete pass of the entire training dataset. Training over multiple epochs allows the model to iteratively learn from the data, adjusting its parameters to improve performance with each pass [44]. The validation

process was applied to tune the model during training, optimize hyperparameters, and help preventing overfitting by monitoring metrics such as validation loss and accuracy.

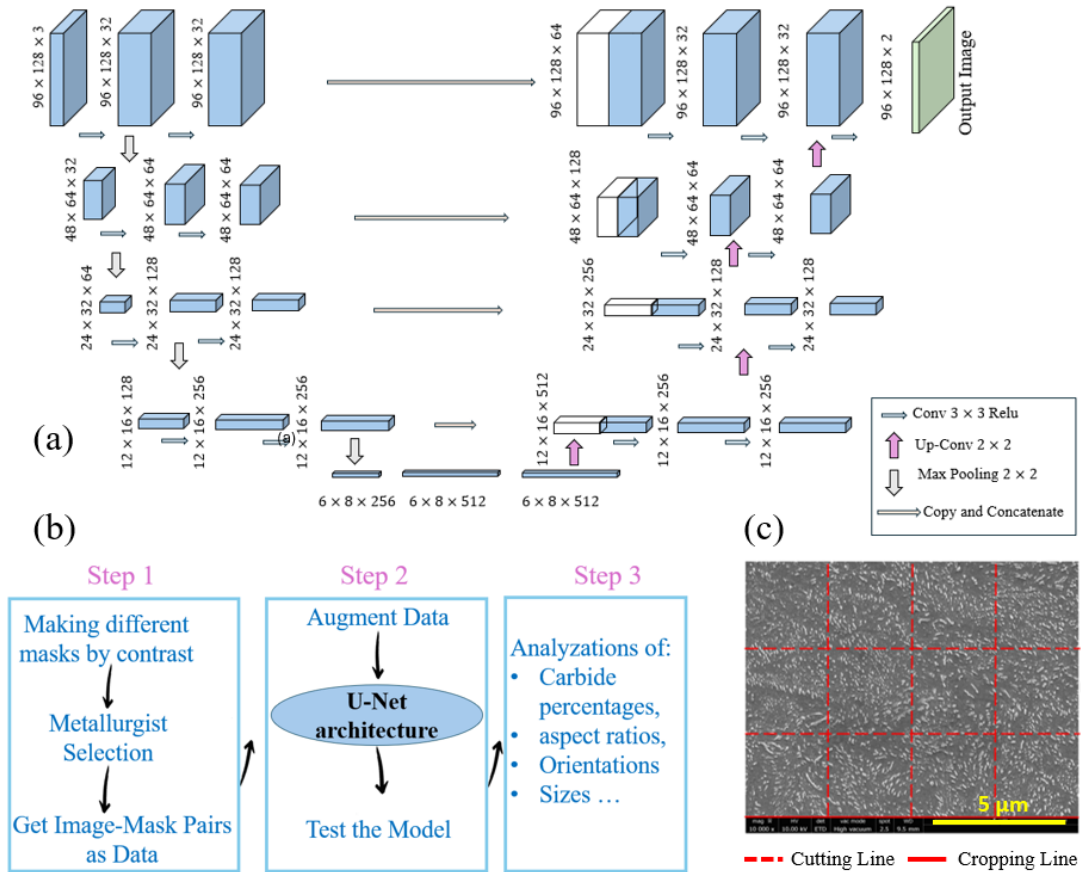


Figure 1. (a) The structure of the U-Net architecture. Each blue box represents a multi-channel feature map. The notation $x \times y \times z$ indicates the dimensions of the image, where x and y are spatial dimensions and z denotes the number of channels. White boxes denote copied feature maps, while the arrows indicate specific operations. (b) fundamental stages for analyzing images. (c) Cropping of original SEM images.

3. Results and Discussion

3.1 Classification of carbides/steel matrix

3.1.1. Model prediction accuracy and loss analysis

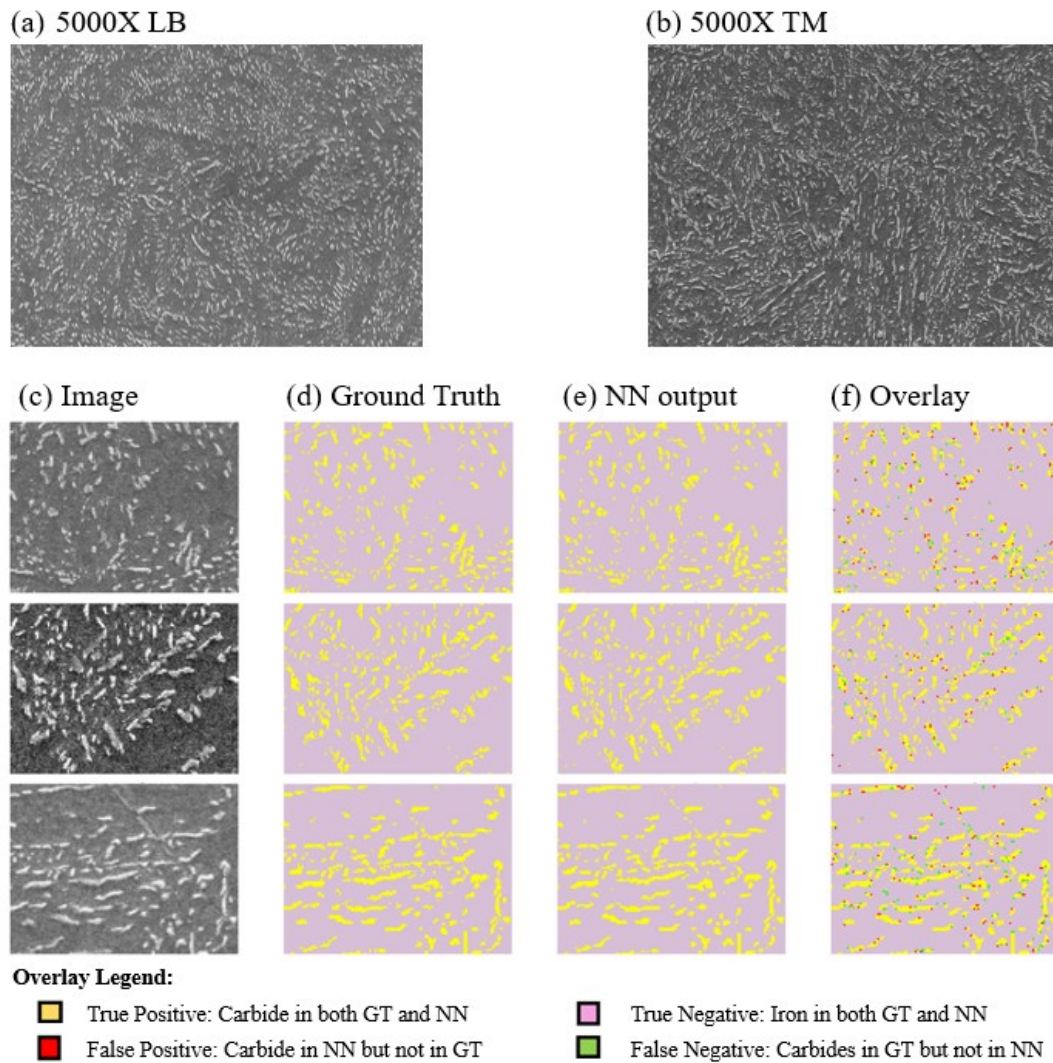


Figure 2: SEM images showing the sample (a) LB and (b) TM microstructures, both at 5000X magnification. (c) Original SEM images and (d) created masks (ground truth), (e) neural network classifications, (f) Overlay of results with legend displayed.

Figures 2a and **2b** present representative SEM images elucidating the LB and TM microstructures respectively. Both microstructures can be seen to feature finely

dispersed carbide precipitates, highlighted by the white regions. Visual comparison shows considerable resemblance between these two microstructures, making their differentiation challenging to naked eyes of non-experts. Utilizing the U-Net framework and workflow we developed, the carbides and steel matrix in both LB and TM microstructures have been classified and analyzed, with some sample classification results displayed in **Figure 2e**. Specifically, **Figures 2c** and **2d** depict the input images (i.e., cropped from the original SEM images) and corresponding ground truth masks, alongside with the predictions made by our DL model in **Figure 2e**. To assess the performance of the DL model, we included images with overlays of the results to illustrate misclassified pixels in **Figure 2f**, specifically highlighting false positives (i.e., carbides predicted by the deep learning model but classified as part of the iron matrix in the masks) and false negatives (i.e., carbides identified in the masks but predicted as part of the iron matrix by the model).

As seen from those overlay images, the DL model effectively captures carbides, with only minor discrepancy observed at the periphery of the carbides (i.e., false positives and false negatives), a region where distinguishing between carbides and the iron matrix is challenging even for metallurgists. This well demonstrates that our model accurately distinguishes carbides, despite being qualitative. To have a quantitative evaluation of our model's performance, we further employed two additional parameters, *accuracy* and *loss*. The *accuracy* parameter is defined as the proportion of correctly classified pixels to the total number of pixels. Meanwhile, for the *loss* parameter, specifically the binary cross-entropy loss function [45], which is widely used to perform binary

classification tasks, is utilized for assessing the model performance. The loss function quantifies the difference between the predicted probabilities and the true labels, defined in **Eq. 1** below:

$$Loss = -\frac{1}{output\ size} \sum_{i=1}^{output\ size} y_i \cdot \log \hat{y}_i + (1 - y_i) \log (1 - \hat{y}_i) \quad (1)$$

Here, y_i represents the label, being 1 and 0 for carbide and iron background pixels respectively. In contrast, \hat{y}_i denotes the predicted probability of a pixel point i being a carbide pixel. The values of *accuracy* and *loss* as the epoch number increases are shown in **Figures 3a** and **3b** respectively. A total of 120 epochs were trained to ensure the convergence of accuracy. It can be noted that the loss values drop abruptly within the first 5 epochs, and after 120 epochs, decrease significantly to 0.041 and 0.047 for the training and validation datasets respectively (cf. **Figure 3a-b**), resulting in an accuracy of 98.3% and 98.1% for training and validation datasets respectively. Additionally, the model's performance was also assessed on the test dataset, with an accuracy of 98.0% attained. These high accuracies attest that our model can successfully learn to classify carbides and the iron matrix with high precision following the training process. One can also note from **Figures 3a** and **3b** that minimizing the cross-entropy loss is crucial in optimizing the model's prediction accuracy.

3.1.2. Model Performance Evaluation via Intersection over Union (IoU)

In addition to the parameters of *accuracy* and *loss*, we also examined another parameter, i.e., the Intersection over Union (IoU). The IoU parameter is a metric commonly used to evaluate how well a predicted region matches the ground truth [46-49]. It proves

particularly valuable in addressing imbalanced tasks, offering a more reliable assessment of spatial overlap compared to accuracy, which often overlooks the impact of localization errors and class imbalances [50]. In our case, IoU is defined as the ratio of the intersection over union between the predicted carbide regions and the ground truth carbide regions (see **Figure 3d**):

$$IoU = \frac{area(C_p \cap C_{gt})}{area(C_p \cup C_{gt})} \quad (2)$$

Here, $C_p \cap C_{gt}$ represents the intersection of the predicted (C_p) and ground truth (C_{gt}) carbide regions, while $C_p \cup C_{gt}$ denotes their union. A high IoU, approaching 1, signifies a substantial overlap between the predicted shape and the ground truth, whereas a low IoU approaching 0 indicates a minimal intersection between the two.

Given the large number of carbide regions in the image, we chose to compute IoU for carbides in each cropped image rather than for individual carbides. To achieve this, we represented the intersection area (i.e., $(C_p \cap C_{gt})$ in **Eq. 2**) as the number of true positive pixels. For the union area (i.e., $(C_p \cup C_{gt})$ in **Eq. 2**), we took the addition of the number of true positive pixels, the number of false negative pixels, and the number of false positive pixels. The outcomes of IoU values for individual images are presented in **Figure 3c**. As depicted in **Figure 3c**, the IoU values for both the validation and test sets closely resemble those of the training set, indicating low variance, suggesting that our model exhibits effective generalization, accurately classifying carbides from SEM images. While most cropped images yield IoU values above 0.85, confirming high accuracy, some images exhibit low IoU values around 0.7, implying that certain mismatch exists between the predicted shape and the ground truth. To understand the

cause leading to the mismatches, we examined those images in detail, with a few representative ones presented in **Figure 4**.

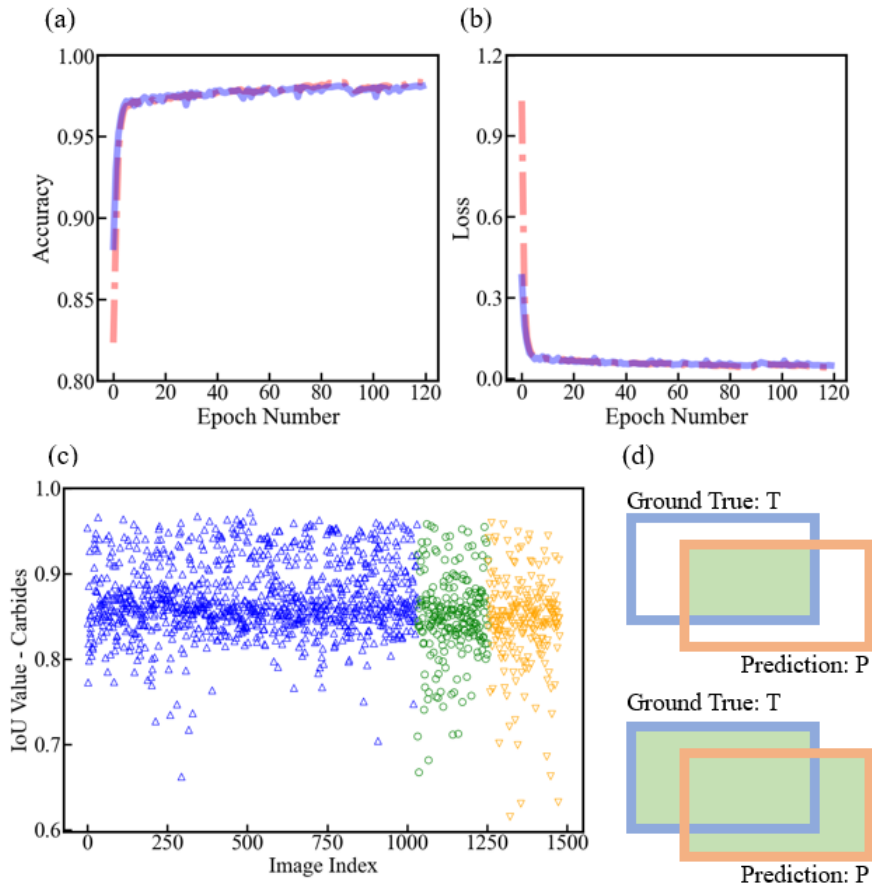


Figure 3 (a) and (b) are accuracy and loss with dash line (solid line) being training (validation) data. (c) The IoU values for each cropped image (Δ , \circ and ∇ represent training, validation, and test data). (d) Schematic illustration of the intersection ($C_p \cap C_{gt}$) (top) and union ($C_p \cup C_{gt}$) (bottom) areas in the definition of IOU (see Eq. (2)).

Figure 4a–c illustrates three representative images with IoU values being 0.68, 0.69 and 0.69. The top rows are superimposed masks and predictions for cropped SEM images. The color scheme is the same as in **Figure 2**, with pink, yellow, green and red regions indicate true negative, true positive, false negative, and false positive. The middle row includes the original SEM images. The bottom row encompasses the superimposed results with the corresponding original SEM images. As illustrated in the

figure, the falsely predicted pixels reveal that these errors primarily occur at the periphery of the carbides. The low IoU can be seen to result from significant presence of false negative pixels in **Figures 4a** and **4b**, while from significant presence of false positive pixels in **Figure 4c**. Notably in **Figure 4a-c**, the microstructures exhibit significant complexity, challenging accurate determination even for experienced metallurgists. Most wrongly-classified pixels occur in edge regions, where even metallurgists find it difficult to confidently determine the correct classification. Therefore, it is equally challenging for AI to distinguish between carbides and the iron matrix in these areas.

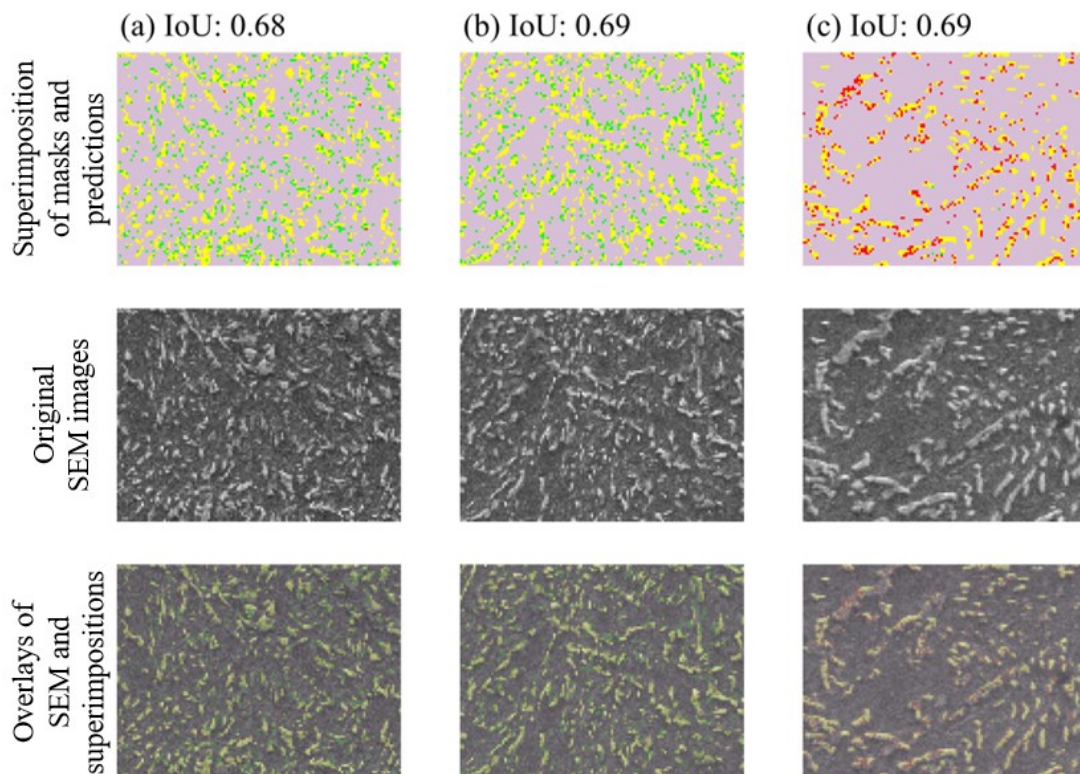


Figure 4 (a-c) Three representative image samples with lower IoU values of (a) 0.68, (b) 0.69, and (c) 0.69. The top row shows the superimpositions of masks and NN predictions, with pink, yellow, green, and red regions indicate true negative, true positive, false negative, and false positive regions. The middle row shows the original cropped SEM images. The bottom row shows the overlays of top row and middle row images.

3.2 Statistical comparison of carbides in LB and TM

3.2.1 Carbide Percentage

The accurate identification of carbides enables us to quantitatively analyze their features, including volume percentage, orientations, and morphology. The carbide percentage can be obtained by dividing the count of NN-predicted carbide pixels, by the total number of pixels within the images, as illustrated in **Figure 5a**. The percentage of carbides in each cropped image, identified by the image index, is plotted in **Figure 6a**, where the blue and purple triangles denote images from the LB and TM microstructures respectively. The carbide percentage distributions are shown in **Figures 6c** for LB and **6e** for TM. As can be noted from the two figures, carbides in both TM and LB exhibit a Gaussian-like distribution. We can also note from the results that the carbide percentages and distributions in LB and TM show great similarity, both exhibiting an average about 0.14 and a standard deviation (STD) of 0.02.

3.2.2 Carbide Orientation and Alignment

In addition to the percentage, we also examined the orientation of carbides, as distinguishing carbide orientations is a crucial strategy for differentiating LB and TM [8]. The examination consists of three steps. First, each carbide was encapsulated in the smallest possible rectangle. To construct the enclosing box, we identified carbide contours using border-following algorithms [51] implemented by OpenCV [52]. The algorithm facilitated the extraction of a sequence of coordinates or chain codes from the border between the connected component of carbide pixels and the connected

component of iron pixels. The bounding boxes were constructed based on the determined contours (see **Figure 5b**). Second, we determined the angle between the longer edge and the horizontal right direction. To ascertain the orientation is unique for each carbide, we calculated the angle to be within a range of -90° to 90° (see **Figure 5b**). Carbide regions (yellow areas in **Figure 5**) with an area smaller than 30 pixels, were classified as noises and thus excluded from the orientation analysis. Third, we gathered the orientation data and designed an alignment factor to characterize carbide orientations. The alignment factor, denoted as k , is calculated according to **Eq. 3** below, for each cropped SEM image:

$$k = \frac{\int_a^b f(x)dx}{\int_{-90^\circ}^{90^\circ} f(x)dx} \quad (3)$$

Here, $f(x)$ represents the number of carbides across different orientations x , spanning from -90° to 90° . We divided carbide orientations into 18 intervals (e.g. -90° to -80° , 80° to 90° for the first and last one) and found out the interval with the greatest number of carbides. The left and right bound of this interval is represented by a and b . The larger the k value, the greater the alignment of the carbides. A higher k value indicates better alignment, and k would approach 1 for near-perfect alignment. One important thing to note is that, given the scale of the cropped image, all the carbides therein primarily reside in a single lath.

The k values of the cropped images are displayed in **Figure 6b**. The outcomes reveal that the alignment factor k in LB and TM SEM images has averages of 0.38 and 0.34 respectively, with comparable STD levels (being 0.07 and 0.06 in LB and TM respectively). The distributions of k values in LB and TM are shown in **Figures 6d** and

6f respectively, both being Gaussian-like, with peak values of 0.35 and 0.32 respectively, while the distribution of k in LB displays a more pronounced tail in the high k range. Overall, the results indicate a more pronounced alignment of carbides in LB compared to TM. This is qualitatively in agreement with what's established in literature studies [8]. However, it is important to note that our results show that statistically the alignment of carbides in LB and TM is only marginally different, not supporting the assertion of carbides in LB tend to exhibit a single variant with an angle of approximately 60° relative to the "growth direction" of the ferrite plate [22, 23].

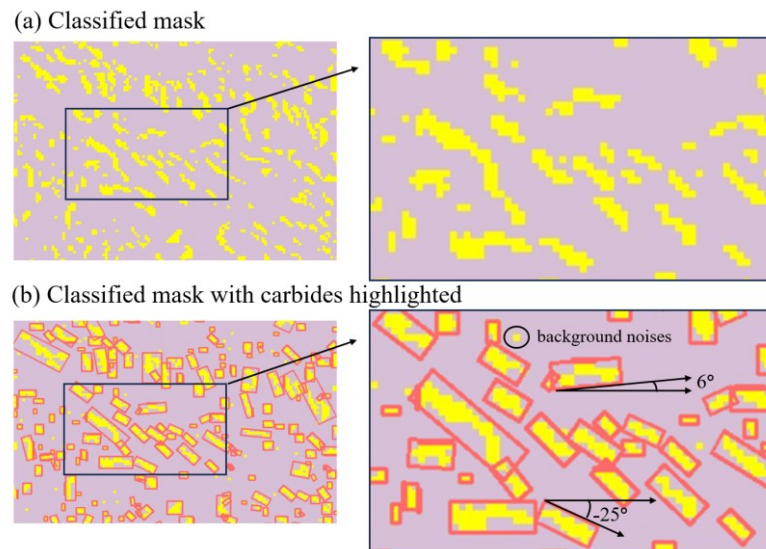


Figure 5 (a) NN classifications of carbides (yellow) and the iron matrix (pink), (b) Carbides are enclosed within defined boundaries (red rectangular boxes) for orientation characterization. The orientation angle is measured relative to the horizontal axis with a range from -90° to 90° .

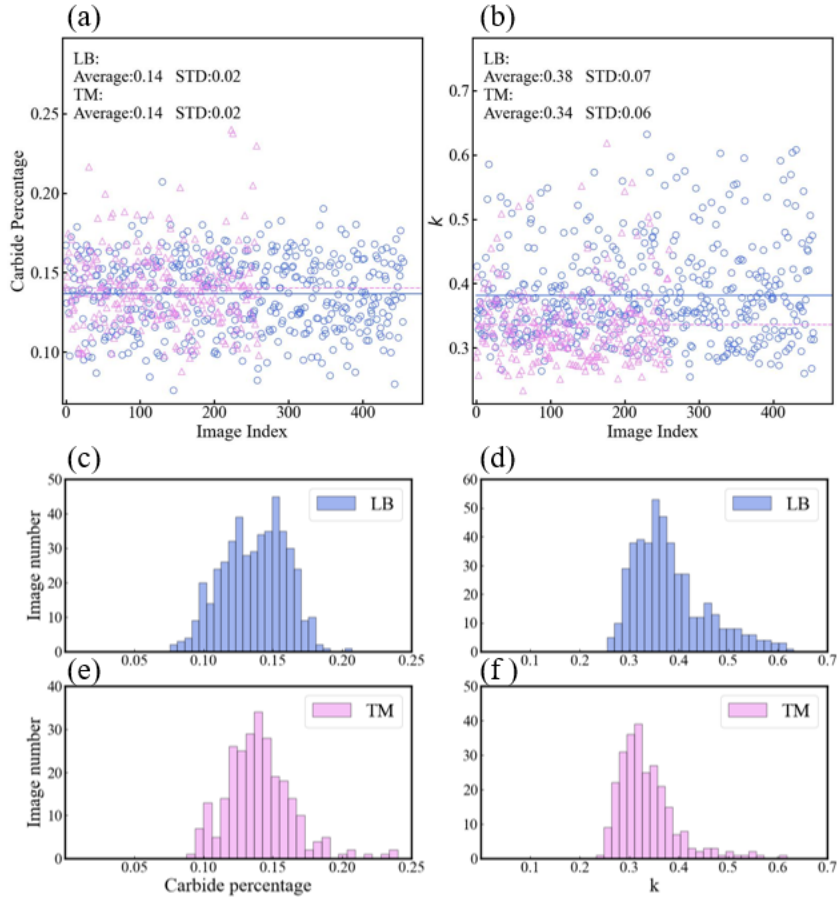


Figure 6 (a) Carbide percentage and (b) the alignment factor k plotted versus the image index. (c) and (e) represent carbide percentage distributions while (d) and (f) are distributions of k in LB and TM respectively.

3.2.2 Carbide Aspect Ratio and Size Distribution

Furthermore, the aspect ratios and size distribution of carbides, which are also important metrics influencing the mechanical properties of HSS [53], have also been analyzed. Specifically, for the aspect ratio, we followed the same steps used in calculating the alignment factor as previously described, where the rectangular boxes enclosing carbides were determined. The value of the aspect ratio was then approximately calculated as the length (the longer edge) and width (the shorter edge) of the rectangular box for each carbide (see **Figure 5b**). The aspect ratio data are shown in **Figures 7a** and **7b** for the cases of LB and TM respectively. The aspect ratios in LB

and TM exhibit the same mean of 1.75, and comparable STD values of 0.72 and 0.70 respectively. Meanwhile, the distributions of aspect ratios are plotted in **Figures 7c** and **7d** respectively for LB and TM, showing great resemblance with very minor difference, both with the carbide aspect ratio predominately between 1.00-2.43. The above results highlight the fact that the LB and TM microstructures have very similar carbide morphologies.

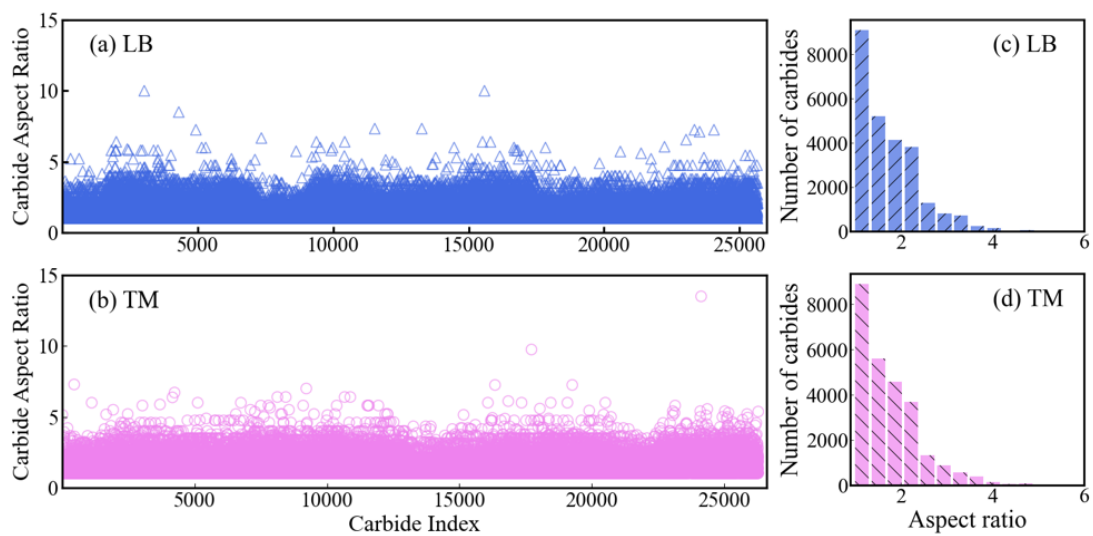


Figure 7. (a-b) The aspect ratios of carbides in LB (Δ) (std: 0.72 and mean: 1.75) and TM (\circ) (std: 0.70 and mean: 1.75). (c-d) Distribution plot of LB ($/$) and TM (\backslash).

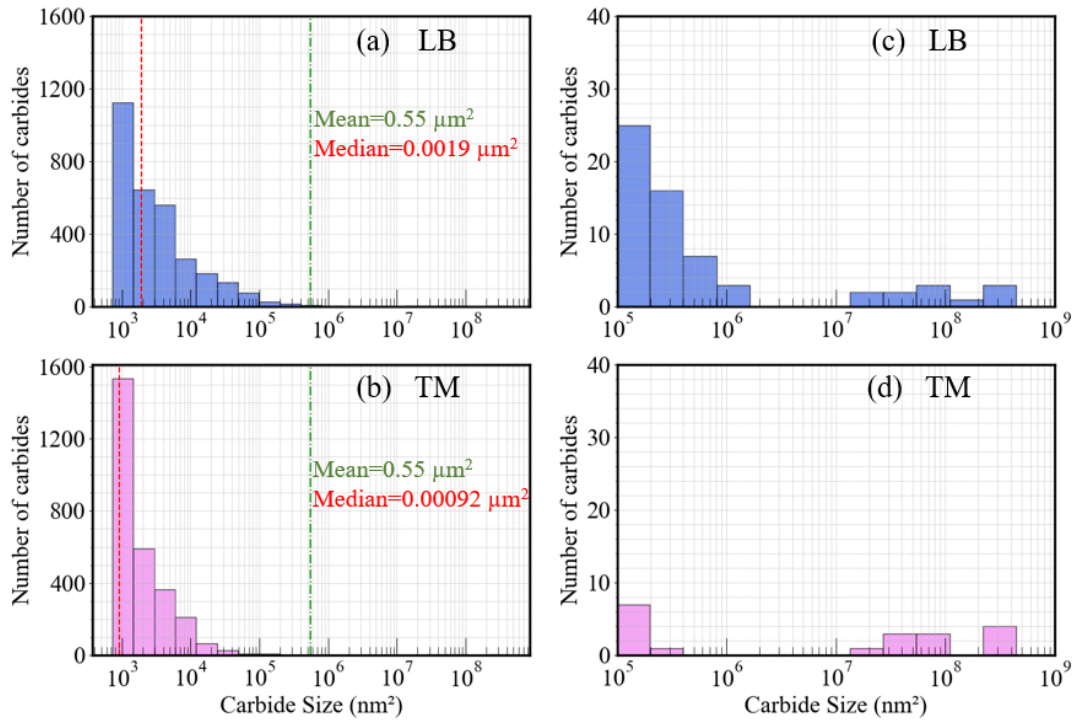


Figure 8 The size distributions of carbides (a) in LB and (b) TM with their respective mean (green dash line) and median (red dash-dot line) size values indicated. (c) and (d) show the number of carbides with size greater than 10^5 nm² in LB and TM respectively.

In addition to the aspect ratio, the sizes of carbides in LB and TM were quantitatively characterized. To ensure precise determination of the carbide size, the small, cropped images were at first amalgamated to the original un-cropped image size, mitigating any errors stemming from the cropping of the carbides. The sizes of carbides are determined by multiplying the number of pixels covering each carbide by the calculated pixel area, with additional details available in the Supplementary Information.

The carbide size distributions are presented in **Figure 8**. Overall, we note that carbides in LB and TM exhibit rather similar half-normal distributions, with nearly the same average size values ($0.55 \mu\text{m}^2$ for LB and TM). However, some notable differences can be observed. Carbides in LB show a broader size distribution than carbides in TM, with more carbides of size larger than $0.1 \mu\text{m}^2$, while in contrast, there is more presence of

fine carbides, of size smaller than $0.0015 \mu\text{m}^2$ in TM. This is also reflected with the median carbide size in LB ($1.9 \times 10^{-3} \mu\text{m}^2$) being significantly larger than that in TM ($9.2 \times 10^{-4} \mu\text{m}^2$).

4 Conclusion

In summary, the present study developed a CNN workflow for comprehensive analysis of carbide precipitates in SEM images of HSS, with a particular emphasis on the LB and TM microstructures. Below list the main findings from this work:

1. A CNN-based DL model specific for differentiating the carbides and iron matrix in SEM images of LB and TM microstructures has been developed, achieving high accuracy (i.e., 98.0% at the pixel level) and efficiency. The model framework is general and thus ready for adaptation to analyze precipitates in other steel systems.
2. Based on the model, statistical analysis has been performed on various aspects of carbide characteristics in LB and TM microstructures, revealing that carbide precipitates in LB and TM share strikingly similarities, exhibiting nearly identical volume percentage, and aspect ratio average and distribution.
3. An alignment factor was defined to enable quantitative analysis of the carbide orientations. Our results showed that overall carbides in LB and TM are both randomly oriented, with carbides showing marginally better alignment in LB than in TM. To the best of our knowledge, our results present the first quantitative statistical comparison of carbide orientations in LB and TM. It is also important to

note that our results are in sharp contrast with the conventional assertion of carbides in LB tend to exhibit a single variant with an angle of approximately 60° relative to the "growth direction" of the ferrite plate. This is significant and cautions against the use of such conventional assertion of carbide orientation as a reliable means to differentiate LB and TM in practices.

4. The carbide sizes in LB and TM also show strong similarities, with almost the same carbide mean size. However, the TM microstructure appears to have a higher percentage of smaller-sized carbides (i.e., carbides with area $< 0.0015 \mu\text{m}^2$).

The present study highlights the effectiveness of CNNs in segmenting SEM images of HSS and differentiating carbide precipitates from the iron matrix with high precision. The results showcased the capability of the DL model as a powerful tool for efficient and quantitative analysis and comparison of steel microstructures, a capability that can be of great value in critical performance assessment, e.g., HE resistance, of steel microstructures in different applications.

Acknowledgements

The authors gratefully acknowledge the Arcelor Mittal Group (AMG) for supplying the materials used in this research. We also acknowledge financial support by Natural Sciences and Engineering Research Council of Canada (NSERC CRDPJ/543696-2019 and RGPIN-2023-03628), and sincerely thank the Digital Research Alliance of Canada for providing the high-performance computing resources. Special appreciation is given to Lucie Leclair for her invaluable contributions through insightful discussions during

the study. Her expertise, guidance, and intellectual input significantly shaped the direction and enhanced the quality of this work.

5 References

- [1] H. Ban, G. Shi, A review of research on high-strength steel structures, *Proceedings of the Institution of Civil Engineers-Structures and Buildings* 171(8) (2018) 625-641.
- [2] M. Takahashi, Development of high strength steels for automobiles, *Shinnittetsu Giho* (2003) 2-6.
- [3] G. Shi, F. Hu, Y. Shi, Recent research advances of high strength steel structures and codification of design specification in China, *International Journal of Steel Structures* 14 (2014) 873-887.
- [4] S. Jenkins, Landing gear design and development, *Proceedings of the Institution of Mechanical Engineers, Part G: Journal of Aerospace Engineering* 203(1) (1989) 67-73.
- [5] R. Kuziak, R. Kawalla, S. Waengler, Advanced high strength steels for automotive industry, *Archives of civil and mechanical engineering* 8(2) (2008) 103-117.
- [6] T. Kamo, R. Ando, M. Sasaki, T. Suzuki, Y. Watanabe, Ultra high strength steel for sustainable building structures, *NSSMC Technical Report* 10 (2015) 65-69.
- [7] F. Badkoobeh, H. Mostaan, M. Rafiei, H.R. Bakhsheshi-Rad, F. Berto, Microstructural characteristics and strengthening mechanisms of ferritic–martensitic dual-phase steels: a review, *Metals* 12(1) (2022) 101.
- [8] H.K.D.H. BHADESHIA, BAINITE IN STEELS, (2015).
- [9] R. Wanhill, R. Byrnes, C. Smith, Stress corrosion cracking (SCC) in aerospace vehicles, *Stress Corrosion Cracking* (2011) 608-650.
- [10] G. Krauss, Martensite in steel: strength and structure, *Materials science and engineering: A* 273 (1999) 40-57.
- [11] D.A. Porter, K.E. Easterling, *Phase transformations in metals and alloys* (revised reprint), CRC press 2009.
- [12] R. Grange, C. Hribal, L. Porter, Hardness of tempered martensite in carbon and low-alloy steels, *Metallurgical transactions A* 8 (1977) 1775-1785.
- [13] J.M. Tartaglia, K.A. Lazzari, G.P. Hui, K.L.J.M. Hayrynen, M.T. A, A comparison of mechanical properties and hydrogen embrittlement resistance of austempered vs quenched and tempered 4340 steel, 39(3) (2008) 559-576.
- [14] H.K.D.H. Bhadeshia, Steels for Rails, Novel, in: K.H.J. Buschow, R.W. Cahn, M.C. Flemings, B. Ilshner, E.J. Kramer, S. Mahajan, P. Veysseyre (Eds.), *Encyclopedia of Materials: Science and Technology*, Elsevier, Oxford, 2002, pp. 1-7.
- [15] J.M. Tartaglia, K.A. Lazzari, G.P. Hui, K.L. Hayrynen, A comparison of mechanical properties and hydrogen embrittlement resistance of austempered vs quenched and tempered 4340 steel, *Metallurgical and Materials Transactions A* 39(3) (2008) 559-576.
- [16] D.E. Hyer-Peterson, Hydrogen embrittlement of 4340 with martensitic and bainitic microstructures for fastener applications, *Colorado School of Mines* 2019.
- [17] N. Nanninga, J. Grochowski, L. Heldt, K. Rundman, Role of microstructure, composition and hardness in resisting hydrogen embrittlement of fastener grade steels, *Corrosion Science* 52(4) (2010) 1237-1246.
- [18] J.W. Jo, H.J. Seo, B.-I. Jung, S. Choi, C.S. Lee, Effect of bainite fraction on hydrogen embrittlement of bainite/martensite steel, *Materials Science and Engineering: A* 814 (2021) 141226.
- [19] F. Saliby, S. Brahimi, S. Rajagopalan, S. Yue, Hydrogen embrittlement susceptibility of bainite

- for high strength steel fasteners, *Materials Performance and Characterization* 6(1) (2017) 462-471.
- [20] B. Sun, D. Wang, X. Lu, D. Wan, D. Ponge, X. Zhang, Current challenges and opportunities toward understanding hydrogen embrittlement mechanisms in advanced high-strength steels: a review, *Acta Metallurgica Sinica (English Letters)* 34 (2021) 741-754.
- [21] S.K. Dwivedi, M. Vishwakarma, Hydrogen embrittlement in different materials: A review, *International Journal of Hydrogen Energy* 43(46) (2018) 21603-21616.
- [22] K.i. Shimizu, T. Ko, Z. Nishiyama, Transmission electron microscope observation of the bainite of carbon steel, *Transactions of the Japan Institute of Metals* 5(4) (1964) 225-230.
- [23] G. Speich, Growth Kinetics of Bainite in a Three Per Cent Chromium Steel, *Decomposition of Austenite by Diffusional Processes: Proceedings of a Symposium Held in Philadelphia, Pennsylvania, October 19, 1960, Under the Sponsorship of the Ferrous Metallurgy Committee of the Institute of Metals Division, the Metallurgical Society, American Institute of Mining, Metallurgical, and Petroleum Engineers, Interscience Publishers, 1962, p. 353.*
- [24] M.-Y. Tu, C.-A. Hsu, W.-H. Wang, Y.-F. Hsu, Comparison of microstructure and mechanical behavior of lower bainite and tempered martensite in JIS SK5 steel, *Materials Chemistry and Physics* 107(2-3) (2008) 418-425.
- [25] J. Feng, M. Wettlaufer, Characterization of lower bainite formed below MS, *HTM Journal of Heat Treatment and Materials* 73(2) (2018) 57-67.
- [26] A. Voulodimos, N. Doulamis, A. Doulamis, E. Protopapadakis, Deep Learning for Computer Vision: A Brief Review, *Computational Intelligence and Neuroscience* 2018 (2018) 1-13.
- [27] K. Simonyan, A. Zisserman, Very deep convolutional networks for large-scale image recognition, *arXiv preprint arXiv:1409.1556* (2014).
- [28] K. He, X. Zhang, S. Ren, J. Sun, Deep residual learning for image recognition, *Proceedings of the IEEE conference on computer vision and pattern recognition*, 2016, pp. 770-778.
- [29] O. Ronneberger, P. Fischer, T. Brox, U-net: Convolutional networks for biomedical image segmentation, *Medical image computing and computer-assisted intervention—MICCAI 2015: 18th international conference, Munich, Germany, October 5-9, 2015, proceedings, part III 18*, Springer, 2015, pp. 234-241.
- [30] H. Zhao, J. Shi, X. Qi, X. Wang, J. Jia, Pyramid scene parsing network, *Proceedings of the IEEE conference on computer vision and pattern recognition*, 2017, pp. 2881-2890.
- [31] J. Redmon, S. Divvala, R. Girshick, A. Farhadi, You only look once: Unified, real-time object detection, *Proceedings of the IEEE conference on computer vision and pattern recognition*, 2016, pp. 779-788.
- [32] H. Law, J. Deng, Cornernet: Detecting objects as paired keypoints, *Proceedings of the European conference on computer vision (ECCV)*, 2018, pp. 734-750.
- [33] M. Larmuseau, M. Sluydts, K. Theuwissen, L. Duprez, T. Dhaene, S. Cottenier, Race against the Machine: can deep learning recognize microstructures as well as the trained human eye?, *Scripta Materialia* 193 (2021) 33-37.
- [34] F. Chollet, *Deep learning with Python*, Simon and Schuster 2021.
- [35] Z. Li, F. Liu, W. Yang, S. Peng, J. Zhou, A survey of convolutional neural networks: analysis, applications, and prospects, *IEEE transactions on neural networks and learning systems* 33(12) (2021) 6999-7019.
- [36] L.-C. Chen, G. Papandreou, I. Kokkinos, K. Murphy, A.L. Yuille, Deeplab: Semantic image segmentation with deep convolutional nets, atrous convolution, and fully connected crfs, *IEEE*

- transactions on pattern analysis and machine intelligence 40(4) (2017) 834-848.
- [37] Y. LeCun, L. Bottou, Y. Bengio, P. Haffner, Gradient-based learning applied to document recognition, *Proceedings of the IEEE* 86(11) (1998) 2278-2324.
- [38] E.A. Holm, R. Cohn, N. Gao, A.R. Kitahara, T.P. Matson, B. Lei, S.R. Yarasi, Overview: Computer Vision and Machine Learning for Microstructural Characterization and Analysis, *Metallurgical and Materials Transactions A* 51(12) (2020) 5985-5999.
- [39] M. Ge, F. Su, Z. Zhao, D. Su, Deep learning analysis on microscopic imaging in materials science, *Materials Today Nano* 11 (2020) 100087.
- [40] O. Ronneberger, P. Fischer, T. Brox, U-Net: Convolutional Networks for Biomedical Image Segmentation, *arXiv pre-print server* (2015).
- [41] L. Tóth, H.-P. Rossmann, T.A. Siewert, Historical background and development of the Charpy test, *European Structural Integrity Society, Elsevier* 2002, pp. 3-19.
- [42] K.L. Scrivener, Backscattered electron imaging of cementitious microstructures: understanding and quantification, *Cement and concrete Composites* 26(8) (2004) 935-945.
- [43] A. Krizhevsky, I. Sutskever, G.E. Hinton, Imagenet classification with deep convolutional neural networks, *Advances in neural information processing systems* 25 (2012).
- [44] I. Goodfellow, *Deep learning*, MIT press, 2016.
- [45] P.-T. De Boer, D.P. Kroese, S. Mannor, R.Y. Rubinstein, A tutorial on the cross-entropy method, *Annals of operations research* 134 (2005) 19-67.
- [46] A. Rosebrock, Intersection over Union (IoU) for object detection, 2016.
- [47] M. Everingham, L. Van Gool, C.K. Williams, J. Winn, A. Zisserman, The pascal visual object classes (voc) challenge, *International journal of computer vision* 88 (2010) 303-338.
- [48] A. Bihani, H. Daigle, J.E. Santos, C. Landry, M. Prodanović, K. Milliken, MudrockNet: Semantic segmentation of mudrock SEM images through deep learning, *Computers & Geosciences* 158 (2022) 104952.
- [49] B. Zhou, H. Zhao, X. Puig, S. Fidler, A. Barriuso, A. Torralba, Scene parsing through ade20k dataset, *Proceedings of the IEEE conference on computer vision and pattern recognition*, 2017, pp. 633-641.
- [50] M.A. Rahman, Y. Wang, Optimizing intersection-over-union in deep neural networks for image segmentation, *International symposium on visual computing*, Springer, 2016, pp. 234-244.
- [51] S. Suzuki, K. be, Topological structural analysis of digitized binary images by border following, *Computer Vision, Graphics, and Image Processing* 30(1) (1985) 32-46.
- [52] G. Bradski, *The OpenCV Library*, Dr. Dobb's Journal of Software Tools (2000).
- [53] D. Casellas, J. Caro, S. Molas, J.M. Prado, I. Valls, Fracture toughness of carbides in tool steels evaluated by nanoindentation, *Acta Materialia* 55(13) (2007) 4277-4286.